International Journal of Heat and Mass Transfer 52 (2009) 1230–1239

Contents lists available at ScienceDirect

International Journal of Heat and Mass Transfer

journal homepage: www.elsevier.com/locate/ijhmt

Vascular materials cooled with grids and radial channels

K.-M. Wang [a], S. Lorente [b], A. Bejan [a,*]

[a] Department of Mechanical Engineering and Materials Science, Duke University, Durham, NC 27708-0300, USA
[b] Université de Toulouse, INSA, LMDC (Laboratoire Matériaux et Durabilité des Constructions), 135, Avenue de Rangueil; F-31 077 Toulouse Cedex 04, France

ARTICLE INFO

Article history:
Received 21 May 2008
Received in revised form 22 August 2008
Available online 30 October 2008

Keywords:
Constructal
Vascular design
Volumetric cooling
Smart materials
Multifunctional
Functionally graded
Grid channels
Radial channels

ABSTRACT

Vascularized materials are a new generation of smart-material concepts that offer novel volumetric functionalities such as self-cooling, self-healing, renewal, cleansing, and "designed" transport properties (permeability, effective thermal conductivity). In this paper, we evaluate the volumetric cooling performance of slabs with embedded flow architectures consisting of grids (G) and radial channels (R). Both flow directions are considered: inlet (I) and outlet (O) in the center of the slab. In total, four configurations (GI, RI, GO, RO) compete for high performance in three directions: (i) low peak of overheating, or low global thermal resistance, (ii) small volume fractions (σ) occupied by high temperatures, and (iii) small pumping power. The results show that grids have lower global flow resistance than radial designs while local junction losses are important. The designs with inlet in the center are attractive in having lower global flow resistance than those with outlet in the center. When objective (i) is considered, designs with outlet in the center are recommended, and the gains in performance are significant if junction losses are negligible and Reynolds numbers are small. For objective (ii), RO is attractive if Sv is greater than 10 or Be is smaller than 10^9. When the three objectives (i)–(iii) are considered at the same time, the configurations with the outlet in the center (GO, RO) are superior when the flow system operates at low pumping power, and that GI and RI are attractive at high pumping power.

1. Introduction

Constructal theory is focusing attention on the relationship between the architecture of the flow system and its global performance. New work and methods for the discovery of effective flow architectures are appearing in several directions that span the landscape from engineering to geophysics, biology and social dynamics [1–13]. This work was revised most recently in Refs. [11–13].

One active direction in engineering is the vascularization of smart materials so that they may offer new or improved volumetric functions: self-cooling, self-healing, variable transport properties, etc. This new generation of smart materials differs from the old in that it has "vasculature by design". The new smart materials look more and more like animal tissues because of the design direction that calls for them and generates them, not because they are copied from nature.

The development of smart materials is marching towards smaller scales and greater interconnectedness between the small-scale details of the structure. Their transformation is driven by the need to install multiple functions throughout the material volume, for example, sensing, actuating, self-cooling, and self-healing. In this direction, the designer of the morphing structure rediscovers the designs of nature: vascularized materials with multi-scale channels and tree-shaped flows, multiple functionality and unmatched robustness.

An important new direction is the development of smart materials with self-healing functionality. Needed is a continuous supply of healing agents throughout the volume of the material. The development of self-healing calls for the vascularization of the entire volume. Supply and evacuation networks are configured and distributed [14,15] in accordance with earliest constructal designs developed for the cooling of electronics [1,2].

In this paper, we consider the use of vasculatures for providing the composite with the ability to experience cooling volumetrically. This is an important departure from the self-healing architectures developed in Refs. [14,15], where the sole objective of the flow architecture was to spread the flow as uniformly as possible through the volume. Here we face the additional challenge of using the flow architecture to cool the body, and to smooth the temperature peaks as much as possible. For this, the facilitation of flow access is an important prerequisite, which is also tied to the pumping power that must be invested in the vascularized composite. To start, we consider two simple flow architectures, embedded grids and radial channels, as a guide for tree-shaped vasculatures later. The search is for results that have fundamental applications in the design of smart vascular structures.

* Corresponding author. Tel.: +1 919 660 5314; fax: +1 919 660 8963.
E-mail address: abejan@duke.edu (A. Bejan).

0017-9310/$ - see front matter © 2008 Elsevier Ltd. All rights reserved.
doi:10.1016/j.ijheatmasstransfer.2008.08.027

Nomenclature

Be	dimensionless pressure drop, Eq. (22)
c_P	specific heat at constant pressure, J kg^{-1} K^{-1}
$d_{g,\,r}$	channel thickness, m
k	thermal conductivity, W m^{-1} K^{-1}
L	the side of the square slab, m
$L_{g,\,r}$	spacing between ports on the perimeter, m
$\dot{m}$	total mass flow rate, kg s^{-1}
n	normal direction
P	pressure, Pa
Pr	Prandtl number, Eq. (21)
q''	bottom heat flux, W m^{-2}
Re	Reynolds number, Eq. (25)
Sv	Svelteness number, Eq. (24)
T	temperature, K
U	mean velocity, m s^{-1}
u, υ, w	velocity components, m s^{-1}
V	total volume, m^3
V_c	total flow volume, m^3
V_{hot}	volume occupied by high temperature, m^3
$\widetilde{W}$	dimensionless pumping power, Eq. (28)
x, y, z	Cartesian coordinates, m

Greek symbols

α	thermal diffusivity, m^2 s^{-1}
ΔP	pressure difference, Pa
ϕ	porosity
μ	dynamic viscosity, kg m^{-1} s^{-1}
ν	kinematic viscosity, m^2 s^{-1}
ρ	density, kg m^{-3}
Σ	summation of pressure drops at junctions
σ	temperature uniformity, Eq. (26)

Subscripts

f	fluid
g	grid pattern
hot	high temperature
in	inlet
out	outlet
max	maximum
min	minimum
r	radial pattern
s	solid

Superscript

$(\tilde{\cdot})$	dimensionless, Eqs. (9)–(12) and (23)

2. Numerical model

Consider a square slab of size $L \times L$ and thickness 0.1 L. The slab is heated from the bottom with the heat flux q'', Fig. 1. The other surfaces are adiabatic. Cooling is provided by an embedded three-dimensional network of cooling channels. Two architectures are modeled and compared: grid and radial (Fig. 1a and b). The spacing between ports on the perimeter is fixed ($L_g = L_r$). The channel thickness of the grids and radial channels are d_g and d_r, respectively. One eighth of the slab with embedded channels is shown in greater detail in Fig. 2.

Two flow directions are considered, from the center of the slab to the periphery, and from the periphery to the center. In total, four flow configurations are explored (see Fig. 1a and b):

GI: grid with the inlet in the center
GO: grid with the outlet in the center
RI: radial channels with the inlet in the center
RO: radial channels with the outlet in the center

Several quantities are fixed in all cases: the volume of the slab (V), the total volume of the flow channels (V_c) (or the porosity $\phi = V_c/V$), and the pressure difference between inlet and outlet (ΔP).

We are interested in flow configurations that shave the temperature peaks (the hot spots) to the lowest levels by using least pumping power. To achieve this, we simulated numerically the fluid flow and temperature fields throughout the volume occupied by solid and flow channels. The conservation equations for mass and momentum are

$$\frac{\partial u}{\partial x}+\frac{\partial \upsilon}{\partial y}+\frac{\partial w}{\partial z}=0, \tag{1}$$

$$\rho\left(u\frac{\partial u}{\partial x}+\upsilon\frac{\partial u}{\partial y}+w\frac{\partial u}{\partial z}\right)=-\frac{\partial P}{\partial x}+\mu\nabla^2 u, \tag{2}$$

$$\rho\left(u\frac{\partial \upsilon}{\partial x}+\upsilon\frac{\partial \upsilon}{\partial y}+w\frac{\partial \upsilon}{\partial z}\right)=-\frac{\partial P}{\partial y}+\mu\nabla^2 \upsilon, \tag{3}$$

$$\rho\left(u\frac{\partial w}{\partial x}+\upsilon\frac{\partial w}{\partial y}+w\frac{\partial w}{\partial z}\right)=-\frac{\partial P}{\partial z}+\mu\nabla^2 w \tag{4}$$

where $\nabla^2 = \partial^2/\partial x^2 + \partial^2/\partial y^2 + \partial^2/\partial z^2$. The conservation of energy in the fluid and solid spaces is expressed by

$$(\rho c_P)_f\left(u\frac{\partial T}{\partial x}+\upsilon\frac{\partial T}{\partial y}+w\frac{\partial T}{\partial z}\right)=k_f\nabla^2 T, \tag{5}$$

$$\nabla^2 T=0 \tag{6}$$

The heat flux imposed from the bottom is

$$q''=-k_s\frac{\partial T}{\partial z} \tag{7}$$

where k_s is the thermal conductivity of the solid. The continuity of heat flux across the solid–fluid interfaces is expressed by

$$k_s\frac{\partial T}{\partial n}=k_f\frac{\partial T}{\partial n} \tag{8}$$

where k_f is the fluid thermal conductivity, and n is the vector normal to the surface. The governing equations were nondimensionalized by defining the dimensionless variables:

$$\left(\tilde{x},\tilde{y},\tilde{z},\tilde{n},\tilde{L}_{g,\,r},\tilde{d}_{g,\,r}\right)=\left(x,y,z,n,L_{g,\,r},d_{g,\,r}\right)/L, \tag{9}$$

$$(\tilde{u},\tilde{\upsilon},\tilde{w})=(u,\upsilon,w)L/\alpha_f, \tag{10}$$

$$\tilde{P}=(P-P_{out})L^2/(\mu\alpha_f), \tag{11}$$

$$\tilde{T}=(T-T_{in})k_f/(q''L) \tag{12}$$

where P_{out} is the lowest pressure (at the outlets), and T_{in} is the lowest temperature (the bulk fluid temperature at the inlets). Written in terms of dimensionless variables, Eqs. (1)–(8) become

$$\frac{\partial \tilde{u}}{\partial \tilde{x}}+\frac{\partial \tilde{\upsilon}}{\partial \tilde{y}}+\frac{\partial \tilde{w}}{\partial \tilde{z}}=0, \tag{13}$$

$$\frac{1}{Pr}\left(\tilde{u}\frac{\partial \tilde{u}}{\partial \tilde{x}}+\tilde{\upsilon}\frac{\partial \tilde{u}}{\partial \tilde{y}}+\tilde{w}\frac{\partial \tilde{u}}{\partial \tilde{z}}\right)=-\frac{\partial \tilde{P}}{\partial \tilde{x}}+\nabla^2\tilde{u}, \tag{14}$$

$$\frac{1}{Pr}\left(\tilde{u}\frac{\partial \tilde{\upsilon}}{\partial \tilde{x}}+\tilde{\upsilon}\frac{\partial \tilde{\upsilon}}{\partial \tilde{y}}+\tilde{w}\frac{\partial \tilde{\upsilon}}{\partial \tilde{z}}\right)=-\frac{\partial \tilde{P}}{\partial \tilde{y}}+\nabla^2\tilde{\upsilon}, \tag{15}$$

$$\frac{1}{Pr}\left(\tilde{u}\frac{\partial \tilde{w}}{\partial \tilde{x}}+\tilde{\upsilon}\frac{\partial \tilde{w}}{\partial \tilde{y}}+\tilde{w}\frac{\partial \tilde{w}}{\partial \tilde{z}}\right)=-\frac{\partial \tilde{P}}{\partial \tilde{z}}+\nabla^2\tilde{w}, \tag{16}$$

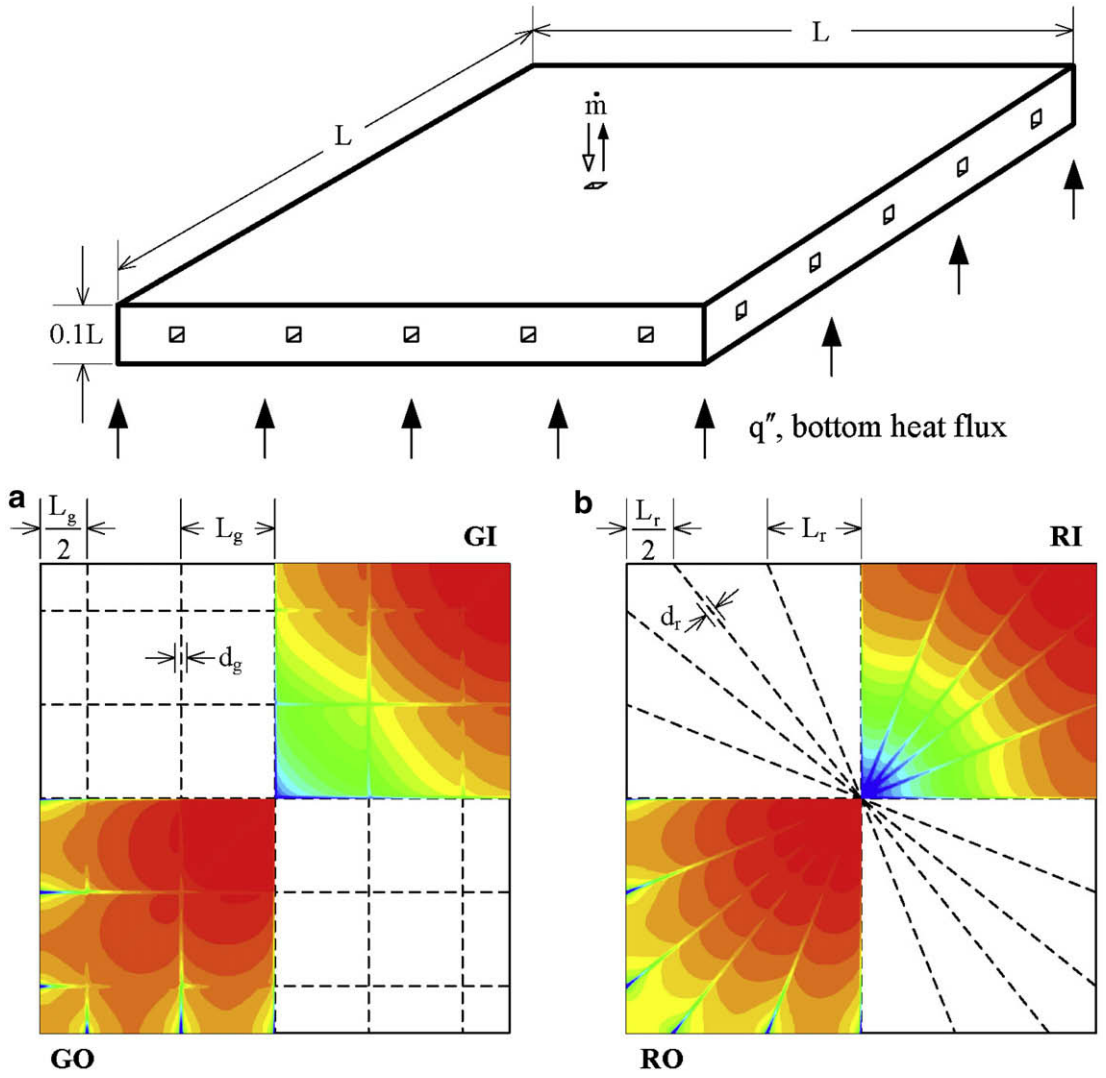

Fig. 1. Slab heated with uniform flux from below; (a) Grid channels; (b) Radial channels. The temperature distributions are the middle planes of the slabs (Sv = 10, Be = 10^{10}).

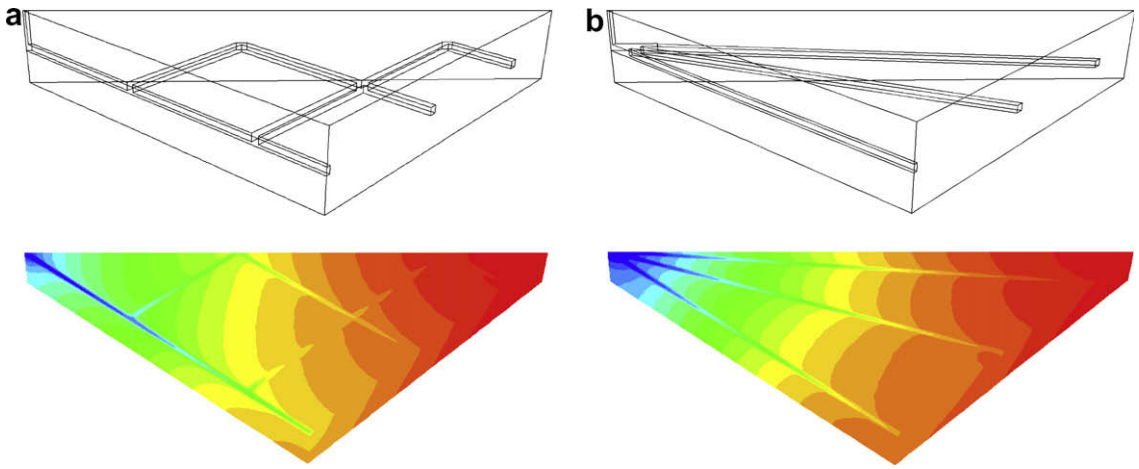

Fig. 2. One eighth of a square slab with embedded channels: (a) grid, (b) radial channels. The upper-left corner is the center of the slab. The temperature distributions are over the surfaces of the bottom half of the slab (Sv = 10, Be = 10^{10}).

$$\tilde{u}\frac{\partial\tilde{T}}{\partial\tilde{x}}+\tilde{v}\frac{\partial\tilde{T}}{\partial\tilde{y}}+\tilde{w}\frac{\partial\tilde{T}}{\partial\tilde{z}}=\nabla^2\tilde{T}, \tag{17}$$

$$\nabla^2\tilde{T}=0, \tag{18}$$

$$1=-\tilde{k}\frac{\partial\tilde{T}}{\partial\tilde{z}}, \tag{19}$$

$$\tilde{k}\left.\frac{\partial\tilde{T}}{\partial\tilde{n}}\right|_{s}=\left.\frac{\partial\tilde{T}}{\partial\tilde{n}}\right|_{f}, \tag{20}$$

where the dimensionless groups are

$$Pr=\frac{\nu}{\alpha_f},\quad \tilde{k}=\frac{k_s}{k_f} \tag{21}$$

The imposed pressure difference ($P_{in}-P_{out}$) gives rise to a third dimensionless group,

$$\mathrm{Be}=\frac{(P_{in}-P_{out})L^2}{\mu\alpha_f} \tag{22}$$

which is the pressure drop number introduced by Bhattacharjee and Grosshandler [16] and Petrescu [17]. The dimensionless total mass flow rate into or out of the slab through the channel at the center of the slab is defined as

$$\tilde{m}=\frac{\tilde{U}\tilde{d}^2_{g,r}}{Pr}=\frac{\dot{m}}{\alpha_f\rho_f L\,Pr} \tag{23}$$

where U is the mean velocity and is nondimensionalized from Eq. (10), and d indicates the channel thickness.

The computations were performed using a finite-volume package [18] with pressure-based solver, least squares cell-based gradient evaluation, SIMPLE algorithm for pressure–velocity coupling and second order upwind scheme for the energy and momentum equations. In order to verify that the solution was independent of grid size, the cell number was increased in steps of 20% until the changes in the total mass flow rate and the maximum temperature were within 1%. The grid was nonuniform such that it was denser in regions where the temperature and velocity fields had higher curvature. The residuals of the continuity equation, momentum equations and the energy equation were less than 10^{-5}. The number of cells used in the simulations varied from case to case, however, the case with the smallest number of cells had more than 0.5 million cells, and the ratio of the cell quantity of solid volume to fluid volume was 1.28–2.11 and 1.09–3.21 for radial and grid structures respectively when the porosity was 0.01.

3. Flow access

The numerical simulations were conducted in the dimensionless parametric domain $Pr = 6$, $\tilde{k} = 18$, $\mathrm{Be} = 10^8 - 10^{10}$. For example, if the physical system consists of epoxy as solid and water as fluid, then these dimensionless parameters correspond to $L = 5$ cm, $\Delta P \sim 5$–500 Pa, $q'' = 10^3 - 10^5$ W/m^2 and hot-spot excess temperatures of order 10^2 K.

The Svelteness of the flow architecture is defined as [19]

$$\mathrm{Sv}=\frac{\text{external flow length scale}}{\text{internal flow length scale}}=\frac{L}{V_c^{1/3}} \tag{24}$$

The Svelteness is a global property of the flow architecture (the "thinness" of the lines of the whole drawing), which shows that when Sv > 10 the effect of pressure losses at the junctions can be neglected. Because the total volume and the flow channel volume are fixed, the porosity ($\phi = V_c/V$) is also fixed. In this paper, we studied $\phi = 0.005$, 0.01 and 0.05, for which the corresponding Sv values are 12.6, 10 and 5.85. The Sv and Be range of these simulations correspond to channels with water flow at Reynolds numbers form 5 to 1000. The Reynolds number is defined as

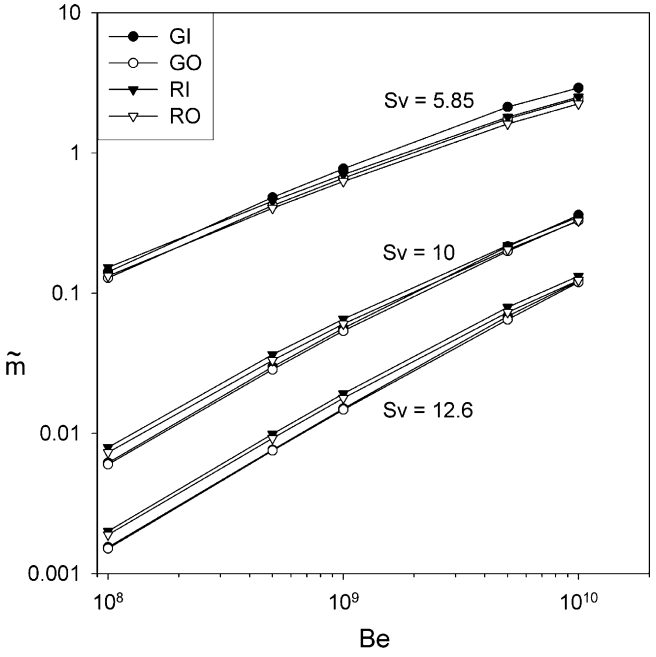

Fig. 3. The total mass flow rate versus pressure drop.

$$Re=\frac{\rho U D_h}{\mu} \tag{25}$$

where D_h is the hydraulic diameter.

Fig. 3 shows how the mass flow rate ($\tilde{m}$) varies with the imposed pressure difference (Be). The four configurations (GI, GO, RI, RO) are defined in the beginning of Section 2. The global mass flow rate $\tilde{m}$ increases with the pressure difference Be, but the relationship $\tilde{m} \sim \mathrm{Be}^n$ depends on Svelteness, with $n = 0.8$, 0.7 and 0.5 for Sv = 12.6, 10 and 5.85, respectively.

The Sv effect is more visible in Fig. 4, where we plotted the ratio $\tilde{m}/\mathrm{Be}$ because in the limit of small Reynolds numbers (small Be and $\tilde{m}$) $\tilde{m}/\mathrm{Be}$ should be constant. In that limit the flow resistance in all

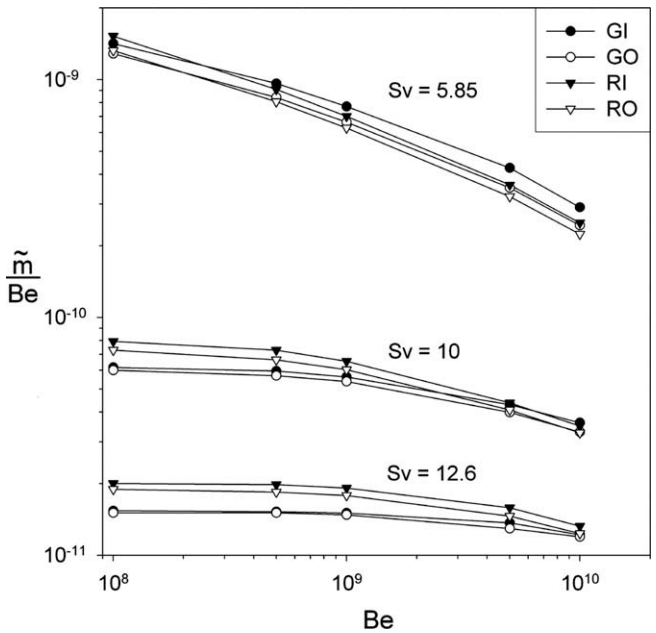

Fig. 4. The deviation of $\tilde{m}(\mathrm{Be})$ from $\tilde{m}/\mathrm{Be} =$ constant.

configurations should be dominated by Poiseuille-flow resistances distributed along the channels. We learn from Fig. 4 that when Sv is smaller than the order of 10, the departure from Poiseuille-type resistance is significant, which means that the effect of local pressure losses (junctions, entrances, etc.) is nonnegligible.

The fluid mechanics problem is to identify designs that provide greater flow access, i.e. smaller global flow resistance. The answer is not clear in Figs. 3 and 4, because for each Sv value the bundle of $\tilde{m}$(Be) curves is tight. Fig. 5 clarifies this issue in two ways. In frames (a) and (b) we see how the ratio $\tilde{m}_{\text{grid}}/\tilde{m}_{\text{radial}}$ varies as Be and Sv change. Because the grid has more junctions than the radial design, we expect the radial design to have lower flow resistance than the grid when junction losses are important, i.e. when Sv is small. However, Fig. 5a and b shows that grids provide greater flow access when local junction losses are important. When Poiseuille-type losses dominate, radial designs provide greater access. This conclusion is valid for both flow directions, inlet in the center and outlet in the center. The explanation lies in the fact that the lone junction in the radial pattern (in the center) is extremely complicated: the channels connect the center with twenty peripheral ports. Compared with this tight bundle of channels near the center, the grids are more simple: they are made by connecting two channels at 90 degrees, and this leads to more manageable junction losses when Sv is not larger than 10.

In frames (c) and (d) of Fig. 5 we evaluated the effect of flow direction on the global mass flow rate when Be and Sv are fixed. The ratio $\tilde{m}_{\text{inlet center}}/\tilde{m}_{\text{outlet center}}$ is greater than 1, more so when Sv is small. In conclusion, for grid and radial designs, the global flow resistance is smaller when the inlet is positioned in the center. Because small Sv means nonnegligible local pressure losses [13,19], the flow direction makes a difference.

To shed more light on the generation of junction losses, we calculated the cross-section averaged pressures before and after the junctions, as shown in Table 1 (Sv = 10, Be = 10^8 and 10^{10}). The locations of these cross-sections are indicated in Fig. 6. From Table 1 we calculated the global measure $\Sigma_{\text{grid}}/\Sigma_{\text{radial}} = 0.19$ (Be = 10^{10}) and $\Sigma_{\text{grid}}/\Sigma_{\text{radial}} = 0.33$ (Be = 10^8), where Σ indicates the summation of all pressure drops at junctions, e.g. $\Sigma_{\text{radial}} = (\widetilde{P}_{\text{j11}} - \widetilde{P}_{\text{j12}}) + (\widetilde{P}_{\text{j11}} - \widetilde{P}_{\text{j13}}) + (\widetilde{P}_{\text{j11}} - \widetilde{P}_{\text{j14}})$. These results show that radial patterns have higher junction losses than grids, however, radial patterns have lower flow resistances along the channels. When junction losses are minor and total junction losses of grids and radial patterns are nearly the same, radial patterns facilitate higher mass flow rates than grids. Figs. 7 and 8 show the pressure distribution along the center of channels. Six routes are defined:

Route 1: Grid, inlet → j11 → j12 → j21 → j22 → j31 → j32 → outlet 1
Route 2: Grid, j23 → j41 → j42 → j52 → j54 → outlet 2
Route 3: Grid, j33 → j51 → j53 → j61 → j62 → outlet 3
Route 4: Radial, inlet → j11 → j12 → outlet 1
Route 5: Radial, j13 → outlet 2
Route 6: Radial, j14 → outlet 3

The slopes of the curves in Figs. 7 and 8 show that radial patterns have lower flow resistance along channels than grids. The pressure drops and recoveries (Fig. 8) result from the secondary flow downstream from the junction.

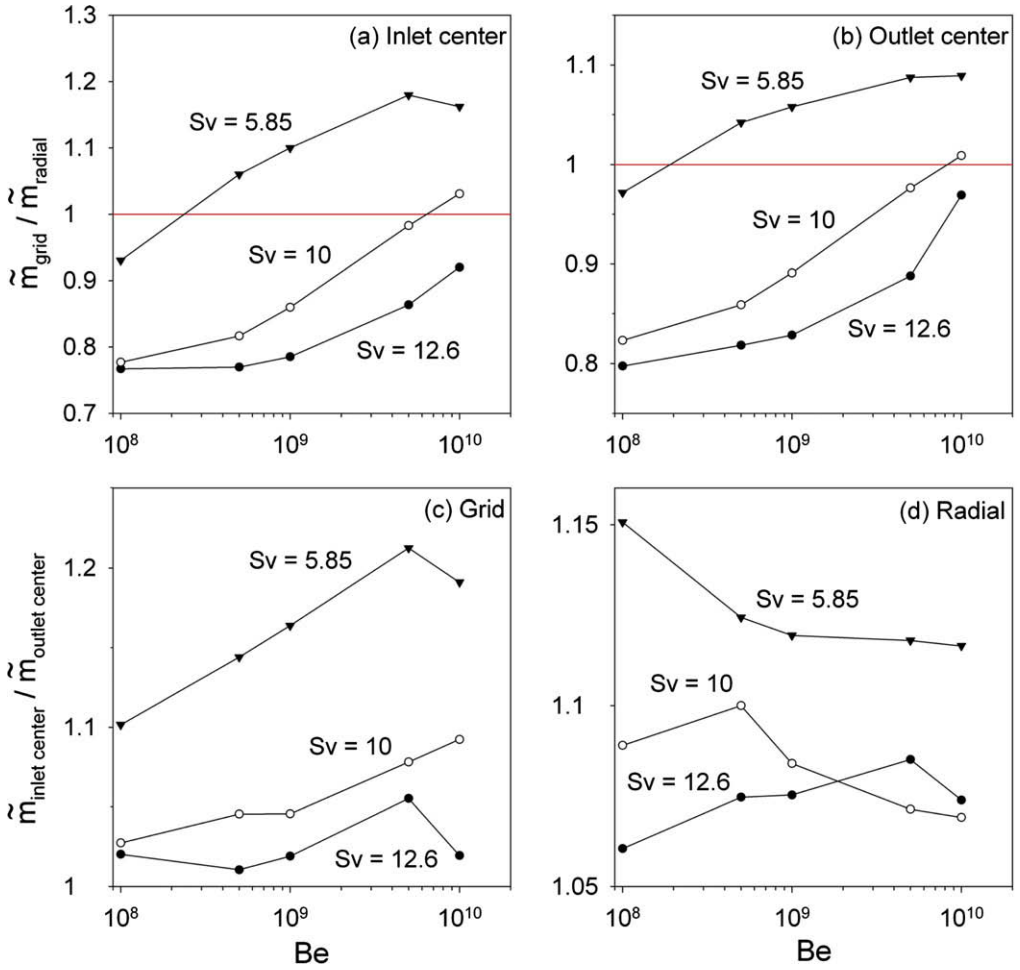

Fig. 5. The effect of flow configuration on the global flow conductance.

Table 1
Cross-section averaged pressures before and after the junction, Fig. 6.

		$\widetilde{P}_{Be=10^8}$	$\widetilde{P}_{Be=10^{10}}$
Grid	j11	6.28×10^7	5.89×10^9
	j12	6.11×10^7	4.27×10^9
	j21	2.41×10^7	1.51×10^9
	j22	2.33×10^7	1.48×10^9
	j23	2.35×10^7	1.35×10^9
	j31	6.63×10^6	4.38×10^8
	j32	6.21×10^6	4.23×10^8
	j33	6.38×10^6	3.98×10^8
	j41	1.41×10^7	8.00×10^8
	j42	1.38×10^7	7.82×10^8
	j51	4.39×10^6	2.58×10^8
	j52	4.50×10^6	2.68×10^8
	j53	4.32×10^6	2.54×10^8
	j54	4.23×10^6	2.53×10^8
	j61	1.50×10^6	8.85×10^7
	j62	1.42×10^6	8.34×10^7
	Σ_{grid}	4.83×10^6	1.92×10^9
Radial	j11	3.68×10^7	4.77×10^9
	j12	3.24×10^7	1.46×10^9
	j13	3.22×10^7	1.45×10^9
	j14	3.11×10^7	1.40×10^9
	Σ_{radial}	1.48×10^7	1.00×10^{10}

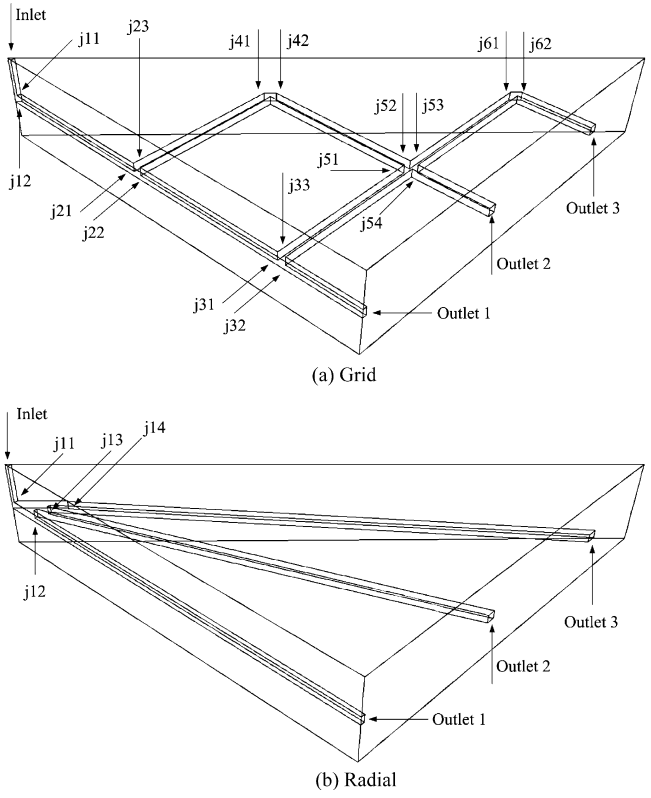

Fig. 6. Notation of surface locations before and after junctions.

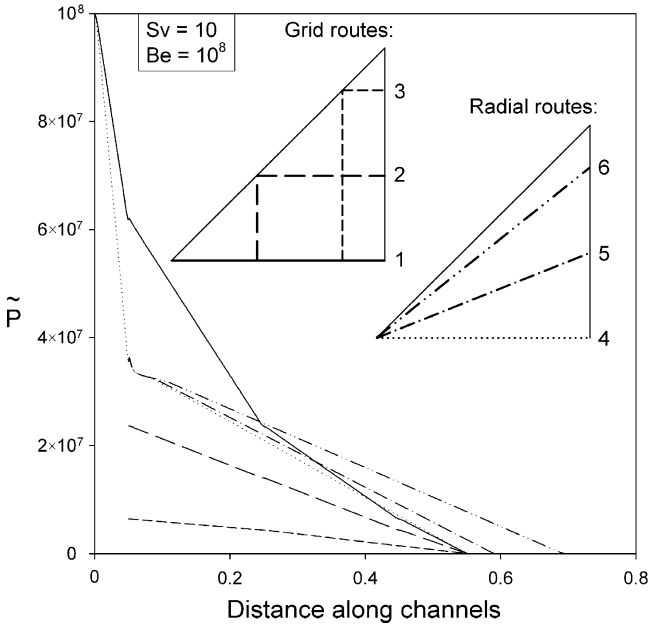

Fig. 7. Pressure distribution along six routes when Sv = 10 and Be = 10^8.

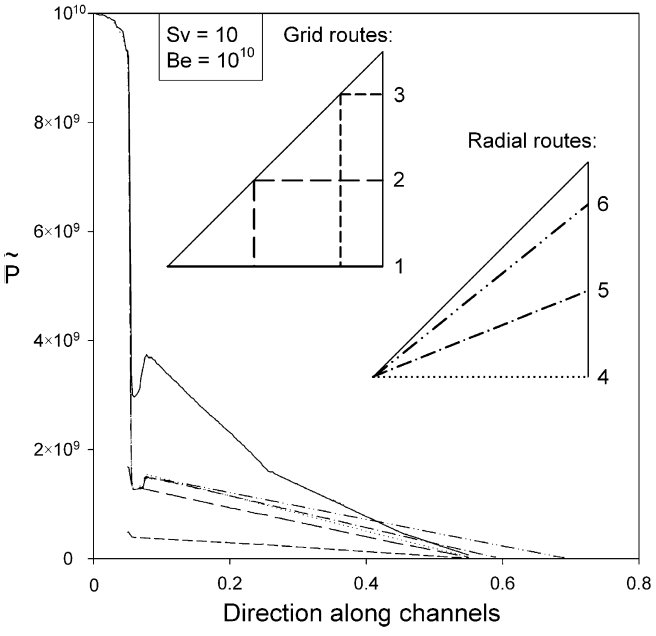

Fig. 8. Pressure distribution along six routes when Sv = 10 and Be = 10^{10}.

We show in Fig. 9a and b details of the velocity distribution near the junction of the radial channels in the center. The left figures are horizontal planes near the junction, in the center of the slab. The right figures are vertical planes passing through the center. As can be seen in Fig. 9a, the fluid flows through the junction smoothly, and the horizontal plane shows the velocity decreases gradually. On the horizontal plane for Be = 10^{10}, the junction flow is illustrated by the velocity concentrated in the left bottom corner, and by the nonuniformity of the velocity distribution in the palm-shaped area. The transition from Fig. 9a to b explains why junction losses are so high when Be = 10^{10}.

4. Hot spots

The temperature distribution in the bottom plane of the square slab is shown in color in Fig. 2. Each triangular slice represents one eighth of the square slab. The center of the slab is the left corner of the triangular slice. Fig. 2a is configuration GI, while Fig. 2b is configuration RI. The color images were computed for Sv = 10 and Be = 10^{10}.

The effect of Be on the maximum excess temperature ($\widetilde{T}_{max}$) is shown in Fig. 10. The positions of the hot spots ($\widetilde{T}_{max}$) are shown in red in Fig. 11, as follows:

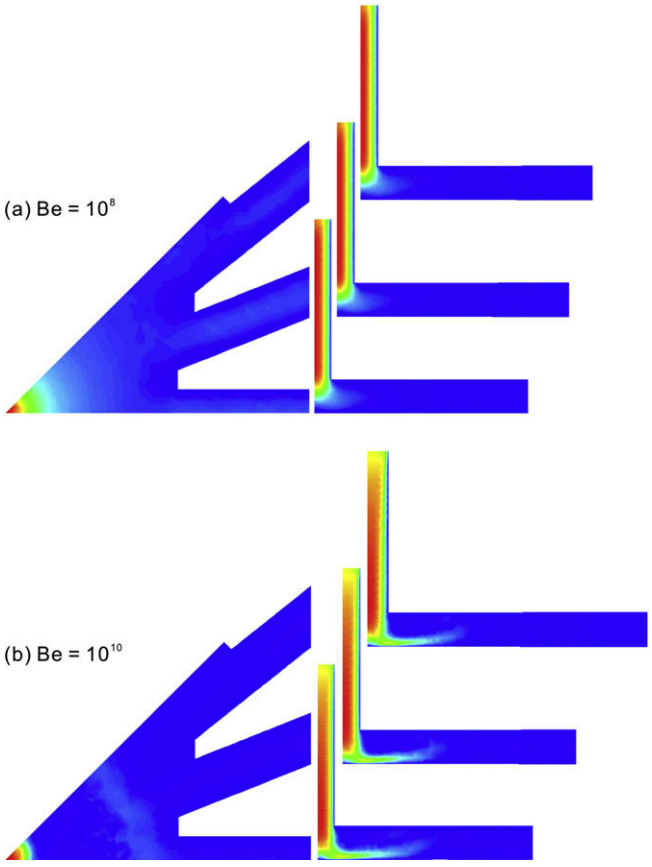

Fig. 9. Velocity distribution of the radial pattern near the junction when Sv = 10 and Be = 10^8, 10^{10}.

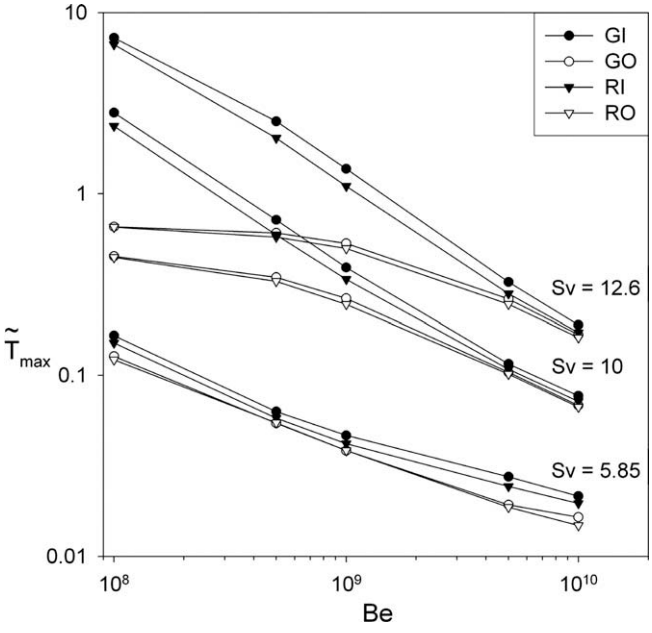

Fig. 10. The effect of flow configuration on maximum local excess temperature.

GI: Corners
RI: Corners
GO: Center
RO: Center

The morphing of configuration is pursued by examining eight cases: two Be values (10^8, 10^{10}) for each of the four configurations (GI, GO, RI, RO). The $\widetilde{T}_{max}$ values of all four configurations converge

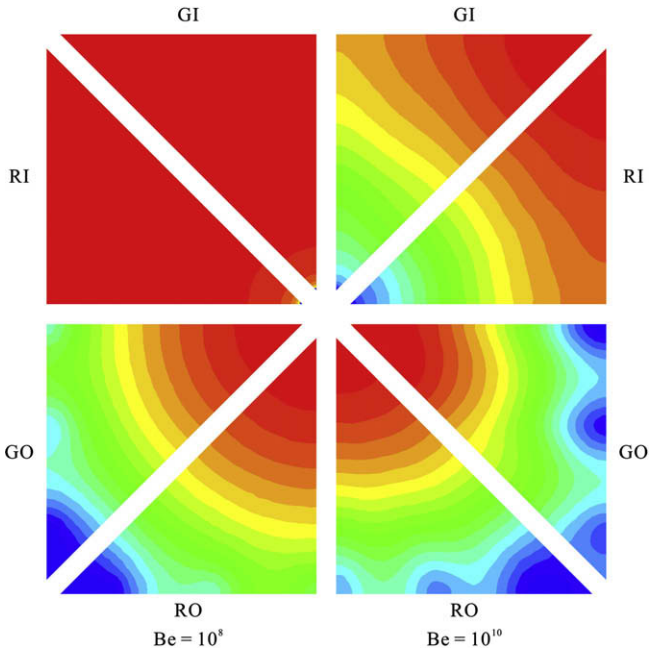

Fig. 11. Temperature distribution in the top plane of four configurations (Be = 10^8, 10^{10}).

to essentially the same limit as Be increases. While Sv is constant, the effect of changing the flow configuration is significant when Be is smaller than 10^9 and Sv is larger than 10, which corresponds to Reynolds numbers smaller than 55 and junction losses are negligible (cf. Fig. 4).

A closer view of configuration on maximum excess temperature is provided in Fig. 12. Frames (a) and (b) show that the ratio $\widetilde{T}_{max,\,grid}/\widetilde{T}_{max,\,radial}$ is greater than 1, indicating that radial designs are superior in the entire (Be, Sv) domain investigated numerically. Frames (c) and (d) show that the ratio $\widetilde{T}_{max,\,inlet\ center}/\widetilde{T}_{max,\,outlet\ center}$ is greater than one for both grid and radial designs. In sum, the better designs for shaving the temperature peaks are those with radial channels and outlet in the center (cf. Fig. 11).

Better cooling architectures are those that have at least two features: (1) lower hot-spot temperatures, and (2) less volume that works at near-T_{max} temperatures. The ability of the four configurations to suppress the maximum temperature [feature (1)] was shown in Figs. 10–12. In order to express feature (2) quantitatively, we propose a new parameter σ,

$$\sigma = \frac{V_{hot}}{V} \tag{26}$$

where V_{hot} is the volume occupied by patches with temperatures ($\widetilde{T}_{hot}$) located between $\widetilde{T}_{max}$ and $\widetilde{T}_{hot}$ ($\widetilde{T}_{hot} < \widetilde{T} < \widetilde{T}_{max}$) such that $\widetilde{T}_{hot}$ approaches $\widetilde{T}_{max}$ within 10 percent,

$$\frac{\widetilde{T}_{max} - \widetilde{T}_{hot}}{\widetilde{T}_{max} - \widetilde{T}_{min}} \leqslant 0.1 \tag{27}$$

Fig. 13 shows how the hot volume fraction σ varies with Be and Sv. Low σ values indicate a body with little volume occupied by high temperatures. The figure shows that configurations with inlet in the center of the slab (GI, RI) are superior to configurations with outlet in the center (GO, RO), provided that Be is larger than 10^9 and Sv is smaller than 10. When the configurations are of type (GO, RO), the bodies vascularized with radial channels have smaller hot volume fractions than bodies with grids, provided that Sv is larger than 10. If the configurations are of type (GI, RI), the improvement derived from choosing between GI and RI is minor.

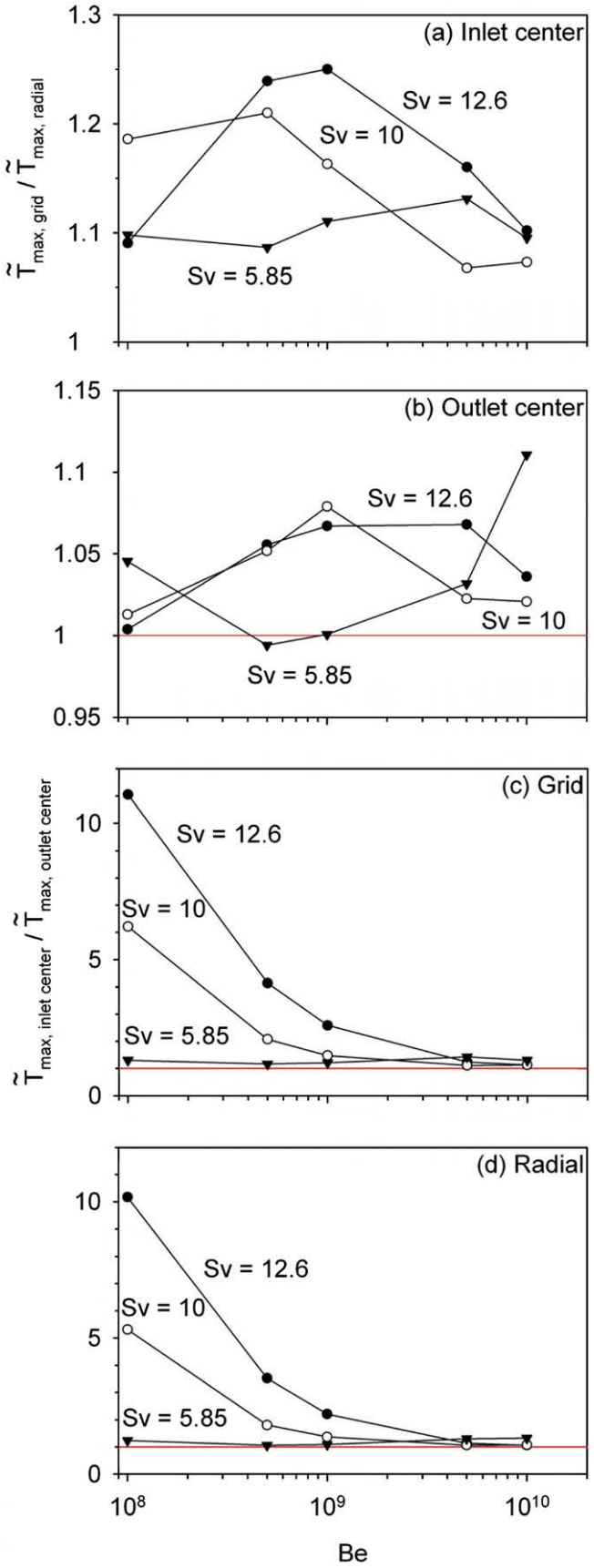

Fig. 12. The effect of flow configuration on the maximum local excess temperature.

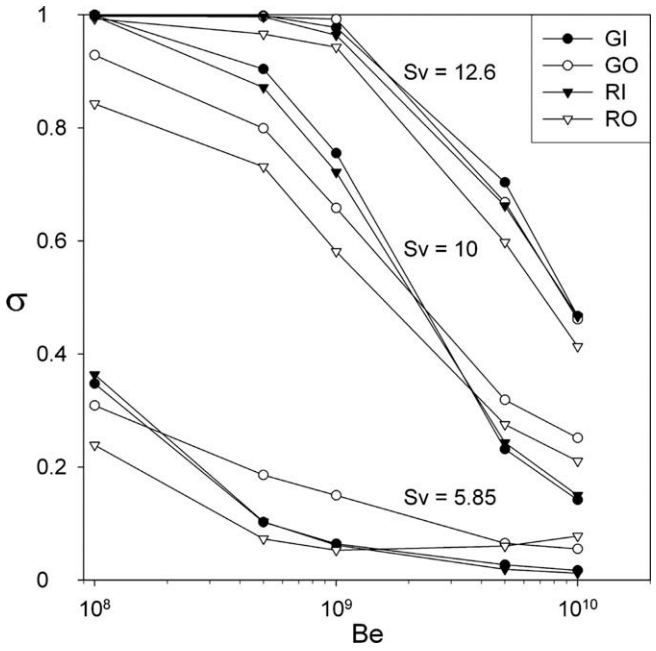

Fig. 13. The effect of flow configuration, Be and Sv on the hot volume fraction.

At small flow rates and pressure drops (Be = 10^8, Sv $\geqslant$ 10) the volumes of configurations with inlet in the center are almost isothermal and at high temperature ($\sigma \simeq 1$). Smaller σ values are preferable. When Sv = 10, the curves cross in the Be range $10^9 - 10^{10}$, such that configurations with inlet in the center are preferable at high flow rates, and configurations with outlet in the center are preferable at low flow rates.

Because embedding channels into composite materials will reduce the material strength, the channel flow volume should be optimized as well. Fig. 13 shows that when $\phi = 0.005$ (Sv = 12.6) the channel flow volume is too small for performing the cooling task: small σ values are possible only when high pressure difference is imposed. On the other hand, when the flow volume is greater, $\phi = 0.05$ (Sv = 5.85), the σ values fall below 0.4 even though a low pressure difference drives the flow.

Most attractive are the vascularized designs that have low $\widetilde{T}_{max}$ and low σ at the same time. In Fig. 14a and b we shows the variation of the highest temperature versus hot volume fraction. Designs that approach the lower-left corner are attractive: GI and RI are preferable when Be = 10^{10} and Sv $\leqslant$ 10. On the other hand, GI and RI are not attractive when Be is as low as 10^8.

5. Pumping power

The thermofluid performance documented until now has a cost, which can be discussed quantitatively in terms of the pumping power that is required by each flow configuration. Because the power required by an isentropic pump is $\dot{m}\Delta P/\rho$, we define the dimensionless pumping power as the product

$$\widetilde{W} = \tilde{m}\mathrm{Be} \tag{28}$$

Fig. 15a and b shows how the cooling objective (low $\widetilde{T}_{max}$ and low σ) is met when the pumping power is specified. The general trend is that $\widetilde{T}_{max}$ and σ decrease as $\widetilde{W}$ increases. One exception is the radial design with outlet in the center (RO) for which σ increases with $\widetilde{W}$ when $\widetilde{W} > 10^9$ and Sv = 5.85.

Attractive are the designs that achieve low $\widetilde{T}_{max}$, low σ and low $\widetilde{W}$ at the same time. These designs are RO and GO for all the cases analyzed in the (Be, Sv) domain covered by this numerical work. Their curves come closest to the lower-left corner of the frames shown in Fig. 15a and b. The RO design is gen-

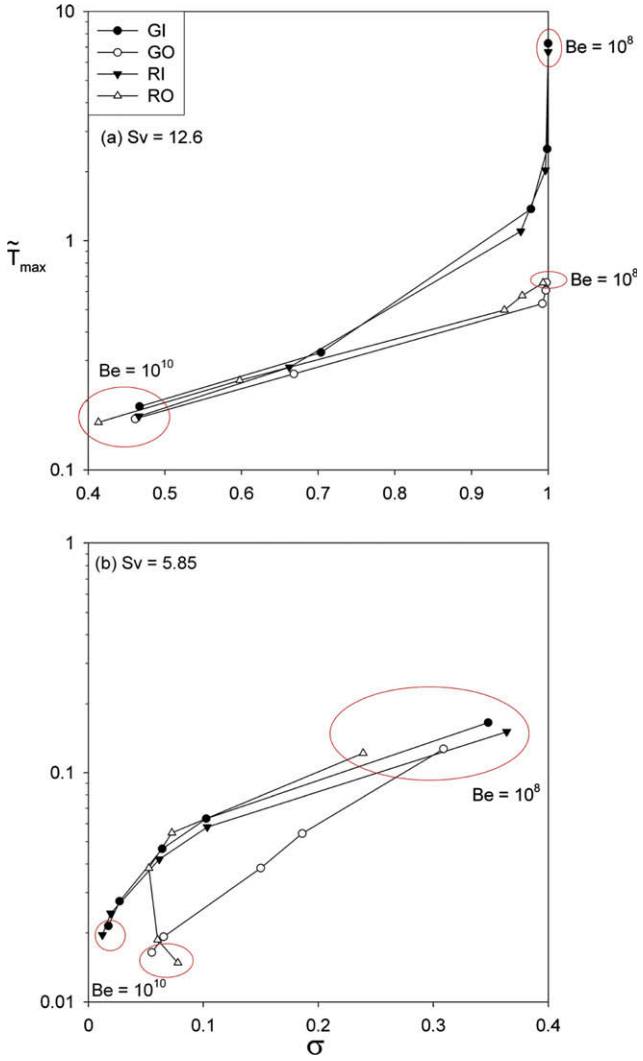

Fig. 14. Two objectives: low excess temperature and low hot volume fraction.

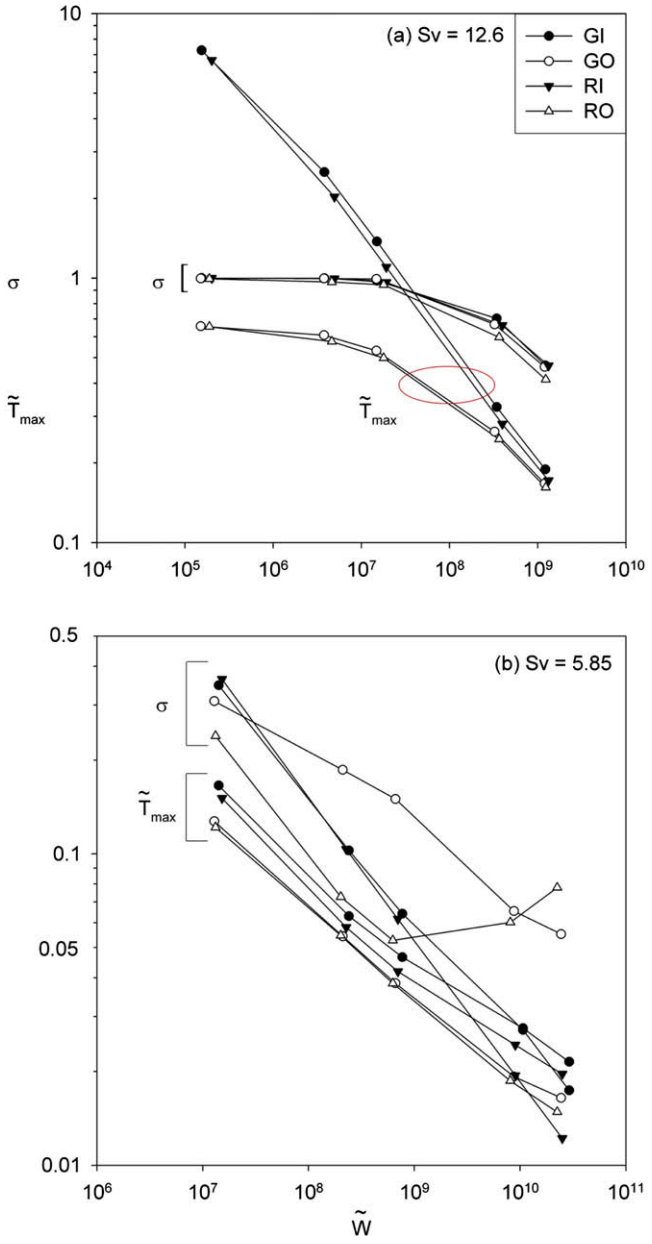

Fig. 15. The effect of pumping power on maximum excess temperature and hot volume fraction.

erally (but slightly) better than GO, with one exception: when Sv = 5.85 and $\widetilde{W} < 10^9$, RO is sensibly better than the other three configurations. When $\widetilde{W} > 10^9$, and Sv = 5.85, the configuration with lowest σ is RI, although the configuration with lowest $\widetilde{T}_{max}$ continues to be RO.

An alternate view of the competition between the four configurations is shown in Fig. 16a and b. The three-dimensional space is $(\widetilde{T}_{max}, \sigma, \widetilde{W})$. When Sv is fixed, each configuration is represented by a curve in this space. The imposed pressure difference increases along each curve, in the direction of increasing $\widetilde{W}$. Attractive are the designs with curves that come closer to the origin of the three-dimensional frame. The relative positions of the curves are more visible in two-dimensional projections (Fig. 15a and b). The merit of Fig. 16a and b is that it shows spatially how the performance changes as the design morphs from GI to GO, RI and RO. Constructal design focuses attention on the three directions simultaneously (low $\widetilde{T}_{max}$, low σ, low $\widetilde{W}$), and this endows the designs with strategy in the search for flow configurations that meet three objectives at the same time.

6. Conclusions

In this paper, we studied the competition of flow configurations in three objectives: low maximum excess temperature ($\widetilde{T}_{max}$), low hot volume fraction (σ) and low pumping power ($\widetilde{W}$). The four flow configurations described in this paper are grid patterns with inlet in the center (GI), grid patterns with outlet in the center (GO), radial patterns with inlet in the center (RI) and radial patterns with outlet in the center (RO).

We found that the effect of local junction losses is negligible while Sv is larger than 10. Low global flow resistance is preferred when self-healing functionality is considered. Results showed that grid patterns are more attractive than radial configurations when local junction losses are important. For both grid and radial designs, patterns with inlet in the center have smaller global flow resistance than configurations with outlet in the center.

For shaving the temperature peaks, configurations with outlet in the center (GO, RO) are superior to those with inlet in the center (GI, RI). The benefits derived from placing the outlet in the center are significant when Reynolds numbers are small and junction losses are negligible. If the objective is to have a low hot volume

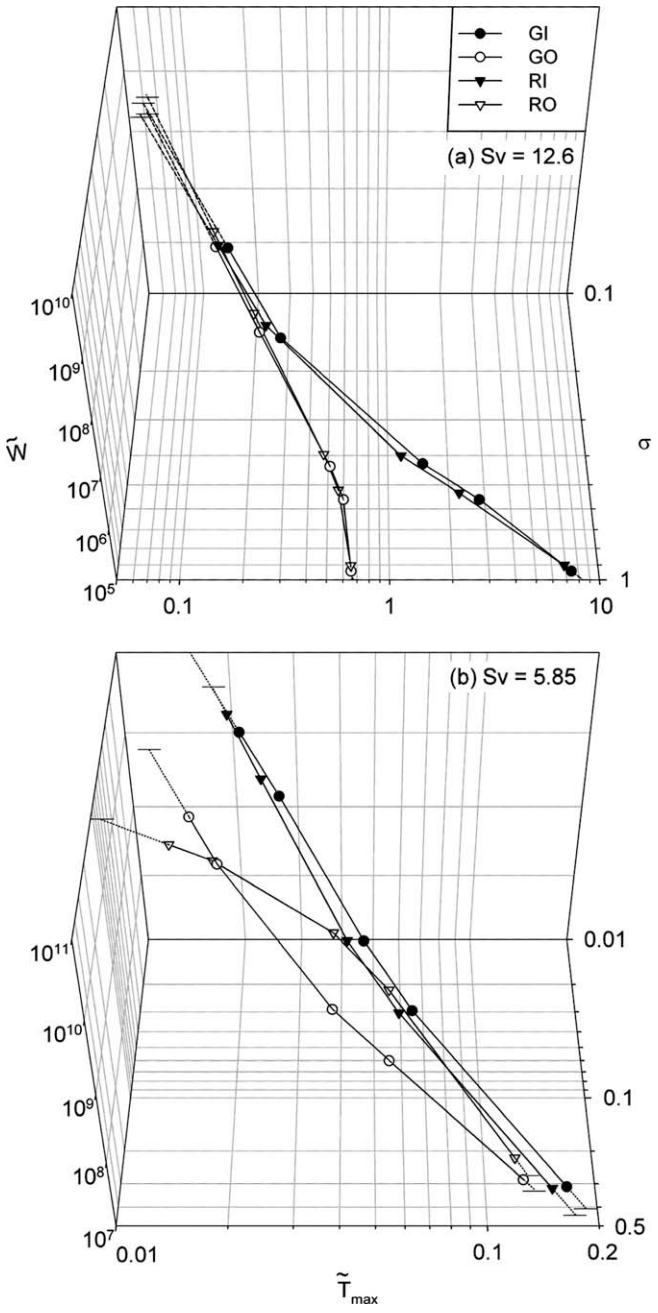

Fig. 16. Three objectives: low excess temperature, low hot volume fraction, and low pumping power.

fraction, RO is the most attractive design when Sv is greater than 10 or Be is smaller than 10^9. In the domain where RO is not attractive, configurations with inlet in the center are superior to those with outlet in the center, and the difference between grids and radial patterns is minor.

When the minimization of pumping power ($\widetilde{W}$) is an objective, we found that $\widetilde{T}_{max}$ and σ decrease as W increases, with one exception that: σ increases while RO is used and $\widetilde{W} > 10^9$ at Sv = 5.85. The results suggested that RO should be applied while $\widetilde{W} < 10^9$. When $\widetilde{W} > 10^9$, RI would be recommended to have low σ, whereas RO is still having the lowest $\widetilde{T}_{max}$ values.

Acknowledgements

This work was sponsored by the Air Force Office of Scientific Research based on a MURI grant for the development of "Micro-Vascular Autonomic Composites" (University of Illinois at Urbana Champaign, Duke University, and University of California at Los Angeles), and based on a grant for "Constructal Technology for Thermal Management of Aircraft". The authors acknowledge with gratitude the advice and guidance received from Dr. David Moorhouse of the Air Force Research Laboratory.

References

[1] A. Bejan, Advanced Engineering Thermodynamics, second ed., Wiley, New York, 1997.
[2] A. Bejan, Shape and Structure, from Engineering to Nature, Cambridge University Press, Cambridge, UK, 2000.
[3] A.H. Reis, A.F. Miguel, M. Aydin, Constructal theory of flow architecture of the lungs, J. Med. Phys. 31 (2004) 1135–1140.
[4] S.M. Senn, D. Poulikakos, Tree network channels as fluid distributors constructing double-staircase polymer electrolyte fuel cells, J. Appl. Phys. 96 (2004) 842–852.
[5] A.H. Reis, Constructal view of scaling laws of river basins, Geomorphology 78 (2006) 201–206.
[6] A. Bejan, J.H. Marden, Constructing animal locomotion from new thermodynamics theory, Am. Sci. 94 (2006) 342–349.
[7] X.-Q. Wang, A.S. Mujumdar, C. Yap, Numerical analysis of blockage and optimization of heat transfer performance of fractal-like microchannel nets, J. Electron. Packag. 128 (2006) 38–45.
[8] V.A.P. Raja, T. Basak, S.K. Das, Thermal performance of a multi-block heat exchanger designed on the basis of Bejan's constructal theory, Int. J. Heat Mass Transfer 51 (2008) 3582–3594.
[9] Y.S. Muzychka, Constructal design of forced convection cooled microchannel heat sinks and heat exchangers, Int. J. Heat Mass Transfer 48 (2005) 3119–3127.
[10] N. Kockmann, T. Kiefer, M. Engler, P. Woias, Channel networks for optimal heat transfer and high throughput mixers, ECI International Conference on Heat Transfer and Fluid Flow in Microscale, Castelvecchio Pascoli, Italy, September 2005.
[11] A.H. Reis, Constructal theory: from engineering to physics, and how flow systems develop shape and structure, Appl. Mech. Rev. 59 (2006) 269–282.
[12] A. Bejan, S. Lorente, Constructal theory of generation of configuration in nature and engineering, J. Appl. Phys. 100 (2006) 041301.
[13] A. Bejan, S. Lorente, Design with Constructal Theory, Wiley, Hoboken, 2008.
[14] A. Bejan, S. Lorente, K.-M. Wang, Networks of channels for self-healing composite materials, J. Appl. Phys. 100 (2006) 033528.
[15] S. Kim, S. Lorente, A. Bejan, Vascularized materials: tree-shaped flow architectures matched canopy to canopy, J. Appl. Phys. 100 (2006) 063525.
[16] S. Bhattacharjee, W.L. Grosshandler, The formation of a wall jet near a high temperature wall under microgravity environment, ASME HTD 96 (1988) 711–716.
[17] S. Petrescu, Comments on the optimal spacing of parallel plates cooled by forced convection, Int. J. Heat Mass Transfer 37 (1994) 1283.
[18] Avaliable from: <www.fluent.com>.
[19] S. Lorente, A. Bejan, Svelteness, freedom to morph, and constructal multi-scale flow structures, Int. J. Therm. Sci. 44 (2005) 1123–1130.